Asian Journal of Chemistry; Vol. 35, No. 5 (2023), 1257-1263

ASIAN JOURNAL OF CHEMISTRY

https://doi.org/10.14233/ajchem.2023.27831

Structural, Optical, Magnetic and Dielectric Properties of $CoFe_{12}O_{19}$ Synthesized in the Presence of *Moringa oleifera* Flower Extract

ABHISHEK A. GOR[1,2,*], MRUNALI JANI[2], ANUP V. SANCHELA[2], N.M. DEVASHRAYEE[3], RAJSHREE B. JOTANIA[4] and CHETNA C. CHAUHAN[1,3,*]

[1]Institute of Science, Nirma University, Ahmedabad-382481, India
[2]Department of Physics, School of Energy Technology, Pandit Deendayal Energy University, Raisan, Gandhinagar-382426, India
[3]Institute of Technology, Nirma University, Ahmedabad-382481, India
[4]Department of Physics, Electronics and Space Science, University School of Sciences, Gujarat University, Ahmedabad-380009, India

*Corresponding authors: Tel: +91 79 23275431; E-mail: abhishekgor5@gmail.com; chetna.chauhan@nirmauni.ac.in

Received: 19 March 2023; *Accepted*: 18 April 2023; *Published online*: 28 April 2023; AJC-21237

In this study, a unique approach was employed to synthesize M-type cobalt hexaferrite ($CoFe_{12}O_{19}$) using *Moringa oleifera* flower extract as a green capping agent. For 3 h, the calcination procedure was conducted at 1100 °C. It was found that the structural, optical, microstructural, magnetic and dielectric properties of the generated cobalt hexaferrite were considerably affected by the presence of phytochemicals in floral extract. To evaluate the structural, surface morphological, optical, magnetic and dielectric properties of prepared ferrite, a variety of characterization techniques including FT-IR, XRD, UV-Vis, SEM, VSM and dielectric techniques were applied. The XRD analysis showed the formation of a hexagonal phase along with hematite and cobalt ferrite, while the surface morphology showed hexagonal shaped platelet structure. With a saturation magnetization (M_s) of 14.94 emu/g and a coercivity (H_c) of 1790.9 Oe, the $CoFe_{12}O_{19}$ powder demonstrated a multidomain nature, which is a magnetically hard material. Furthermore, the energy bandgap of the cobalt ferrite was observed to be 2.01 eV. Low frequency dielectric measurement was carried out at room temperature and $\varepsilon'_{max} \sim 46$ found at 30 Hz with tan δ equals to 0.103. The dielectric behaviour with frequency follows the Koop's model and Maxwell-Wagner theory. One semicircle arc was observed in Cole-Cole plot.

Keywords: *Moringa oleifera*, $CoFe_{12}O_{19}$ hexaferrite, Green synthesis approach, Dielectric measurements.

INTRODUCTION

The M-type metal hexaferrite ($MFe_{12}O_{19}$) hexagonal ferrites (where M is Ba, Sr, Ca, *etc.*) have been investigated since the 1950s and have been the subject of numerous studies due to their unique properties and commercial applications [1]. The magnetism that hexaferrites exhibit, which is brought on by the unique crystalline structure of these materials, is one of their most significant characteristics. Owing to this feature, hexaferrites have a wide range of uses such as transformer cores, permanent magnets, memory devices and magnetic imaging pigments. There are six groups of hexaferrites categorized as M, Z, Y, X, W and U-type ferrites [2]. Various methods have been used to synthesize hexaferrites, but the sol-gel method is the most convenient method due to its ability to control the size and morphology of the final products. This method is eco-friendly and does not require expensive equipment since it uses green solvents [3].

Recently, green synthesis route has been used to synthesize hexaferrites using natural sources such as carbohydrates, pigments, amino acids and microorganisms as reducing agents. Although cobalt-containing hexaferrites have been widely studied, cobalt hexaferrite nanoparticles are synthesized using natural reducing agents that have not been synthesized earlier or have been less considered [4]. *Moringa oleifera* flower extract has been identified as a potential source for green synthesis. The flowers of *Moringa oleifera* are rich in bioactive compounds, including flavonoids, phenolic acids and alkaloids [5]. These compounds have also been shown to possess antioxidant, antimicrobial and anticancer properties. The use of *M. oleifera* flower extract for green synthesis is environmentally friendly and does not involve the use of toxic chemicals. Several studies

[6-9] have reported the use of *M. oleifera* flower extract for green synthesis. Its extract, for instance, is used to create silver nanoparticles, which have good antibacterial properties against *Staphylococcus aureus* and *Escherichia coli*. Similarly, there is a study where the extract is used to synthesize gold nanoparticles, which showed potent anticancer activity against breast cancer cells [10].

EXPERIMENTAL

The first phase of the experiment involved collecting fresh flowers of *Moringa oleifera*, which were collected from local garden and washed twice with distilled water to clean. The flowers were dried in open air and then 10 g of flowers were boiled in 200 mL of deionized water for 30 min at 80 ºC followed by cooling to room temperature. The resulting solution was subjected to filtration using Whatman's paper filter no. 42 to obtain an extract of *Moringa oleifera* flowers. *Moringa oleifera* flower extract was mixed with stoichiometric amounts of cobalt nitrate ($Co(NO_3)_2{\cdot}6H_2O$, 99.0% pure) and iron(III) nitrate nonahydrate ($Fe(NO_3)_3{\cdot}9H_2O$, 99% pure). The resulting mixture was vigorously stirred at room temperature on a magnetic stirrer for 1 h to ensure homogeneity. The homogeneous mixture was then heated in an oil bath at 100 ºC while being regularly agitated until it changed into brownish dried precursors. The dried precursors were pulverized with a mortar and pestle after being allowed to cool to room temperature. The powder was calcined in a muffle furnace for 3 h at 1100 ºC. The $CoFe_{12}O_{19}$ (CoM) ferrite was produced by stabilizing the resulting powder at room temperature.

RESULTS AND DISCUSSION

FTIR studies: FTIR analysis was used to examine the type of carbon residue and metal oxide bond formation in the prepared CoM ferrite. The spectrum was captured at a wavenumber range of 4000 to 400 cm^{-1} at 300 K using a Perkin-Elmer FT-IR spectrometer (Fig. 1). The absorption band at ~ 568 cm^{-1} (ν_1) indicates the tetrahedral group, while the absorption bands ~ 463 (ν_2) and 409 cm^{-1} (ν_3) represent the octahedral group [11]. The band (ν_1) at the tetrahedral (A) site, denotes Fe^{3+}- O^{2-} stretching vibrations, whereas the band (ν_2) denotes trivalent metal-oxygen (M-O) vibrations at the octahedral (B) site. Due to its short bond length, the tetrahedral cluster (ν_1) has a greater vibrational mode than the octahedral clusters (ν_2) do [12]. A lower band, (ν_3) at lower wavenumber ~ 409 cm^{-1}, which is related to the divalent Co^{2+}–O^{2-} bond in the complex.

XRD studies: Fig. 2 represents the XRD pattern of the $CoFe_{12}O_{19}$ ferrite synthesized using *M. oleifera* flowers extract. The XRD pattern was captured using a Bruker D Z Phaser diffractometer (Model-PW 1830, $\lambda = 1.5405$ Å, with scan rate 2º/min). The synthesis of CoM was first reported by Ansari *et al.* [13] and when the observed XRD peaks were compared to those

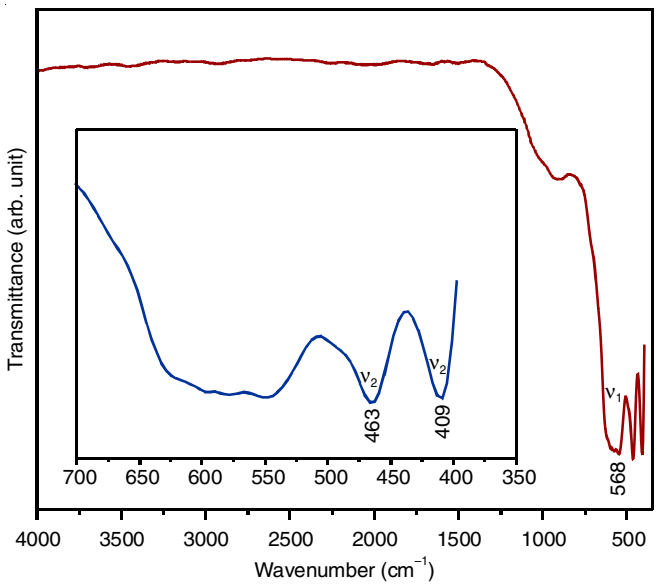

Fig. 1. FTIR spectrum of $CoFe_{12}O_{19}$ sample

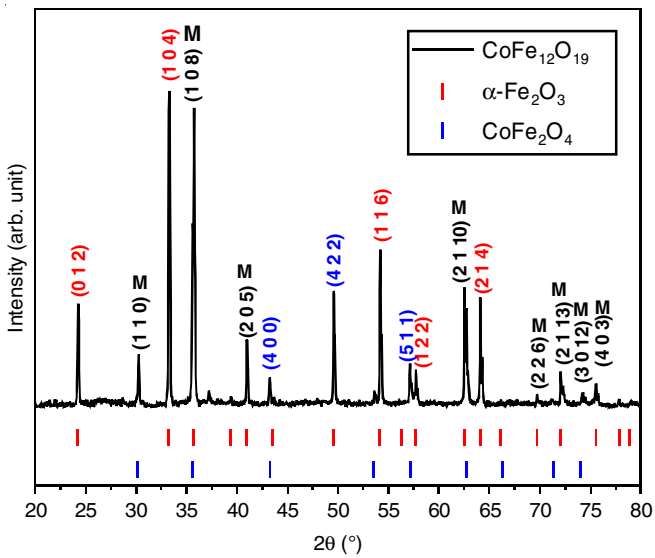

Fig. 2. XRD pattern of $CoFe_{12}O_{19}$ sample

on JCPDS card No. 43-0002 for barium (BaM), strontium (SrM) and lead (PbM) hexaferrite, it was determined that the diffraction line sites of the hexaferrite compounds were similar. By comparing the diffraction lines of the CoM XRD pattern with the diffraction lines of other hexaferrites, it is possible to verify that $CoFe_{12}O_{19}$ formed in this study. The powder-X software was used in indexing diffraction lines, which were matched with standard peaks of $BaFe_{12}O_{19}$ hexaferrite (card no: 00-043-0002, space group $P6_3/mmc$, a = b = 5.8920 Å, c = 23.1830 Å and V = 696.99 $Å^3$), $CoFe_2O_4$ (PDF file No: 000021045) and α-Fe_2O_3 (PDF file No: 000130534). The planes of diffraction (0 1 2), (1 1 0), (1 0 4), (1 0 8), (2 0 5), (4 0 0) (4 2 2) (1 1 6),

TABLE-1
LATTICE PARAMETERS (a,c), UNIT CELL VOLUME (V) AND CRYSTALLITE SIZE (D_{XRD}) OF $CoFe_{12}O_{19}$ SAMPLE, PREPARED IN PRESENCE OF *Moringa oleifera* FLOWERS EXTRACT AND HEATED AT 1100 °C FOR 3 h

Sample	a (Å)	c (Å)	c/a	V $(Å)^3$	2θ (°)	D_{XRD} (nm)
$CoFe_{12}O_{19}$	5.8998	23.1104	3.91	720.03	33.32	12.04

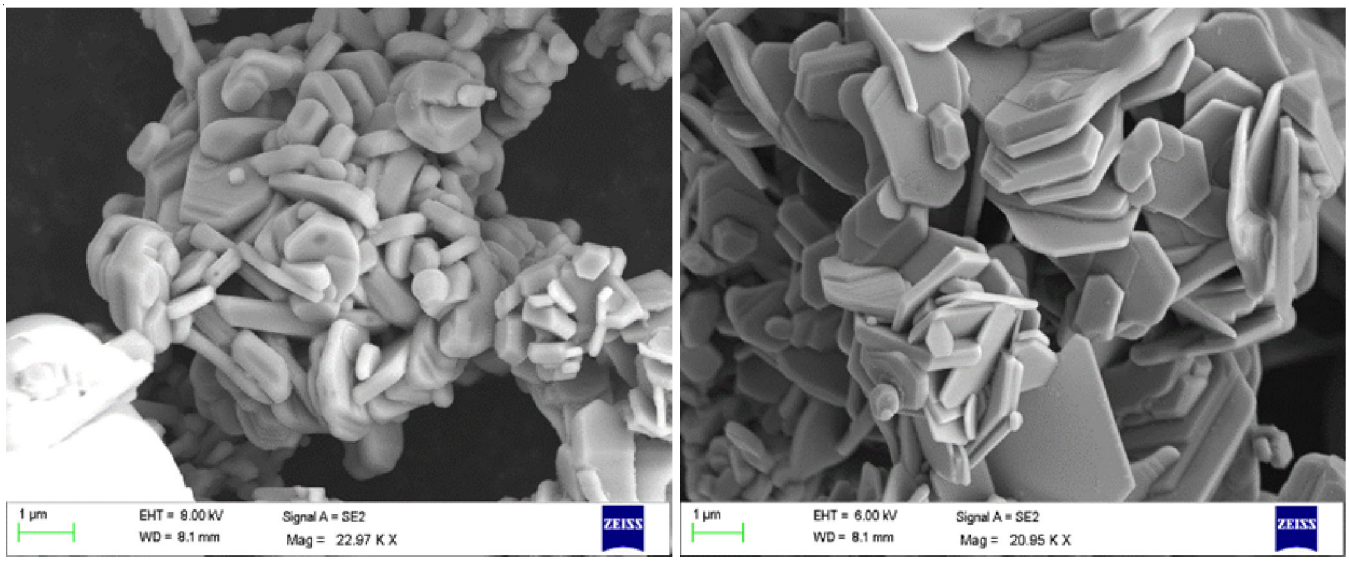

Fig. 3. SEM Micrographs of $CoFe_{12}O_{19}$ hexaferrite sample with different magnification

(5 1 1), (1 2 2), (2 1 10), (2 1 4), (2 2 6), (2 1 13), (3 0 12), (4 0 3), were observed in present sample. Lattice parameters, *c/a* ratios, cell volume and crystallite size of $CoFe_{12}O_{19}$ are listed in Table-1. The XRD analysis shows the presence of M (50%), hematite (α-Fe_2O_3 31.25%) and $CoFe_2O_4$ (18.75%) phases.

Surface morphology: Using Zeiss scanning microscopy, the surface morphology of CoM hexaferrite was investigated, as shown in Fig. 3. From the micrographs, it is evident that prepared CoM ferrite exhibits hexagonal platelets morphology, as expected from crystal structure [14], which consists of stacked hexagonal layers. The platelet shape may also be influenced by the specific synthesis condition used to prepare CoM ferrite in presence of *Moringa oleifera* flower extract as a biogenic reducing agent [15].

Optical properties: The UV-VIS-NIR absorption spectra (Fig. 4) were obtained at room temperature in the wavelength range of 200 to 1200 nm using a UV-2600i Shimadzu UV-VIS Spectrophotometer. Strong and weak absorption zones, as well as an absorption edge, are visible in the absorption spectrum. The band gap is created by the high absorption edge at 620 nm.

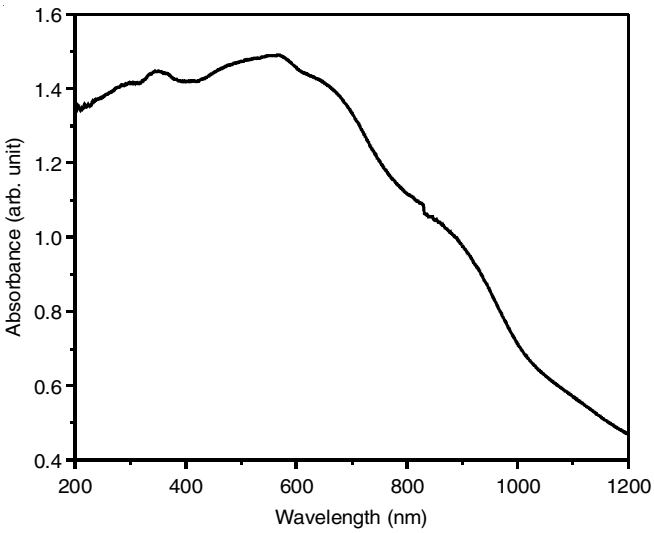

Fig. 4. UV-VIS-NIR absorbance spectrum of $CoFe_{12}O_{19}$ sample

The band gap was calculated using the Tauc plot in Fig. 5. The Tauc relation (eqn. 1) is used to calculated bandgap at 2.01 eV [16].

$$\alpha h\nu = K(h\nu - E_g)^n \quad (1)$$

where α is the material's absorption coefficient, $h\nu$ is the energy of a photon, K is constant, E_g is the average band gap of material and n depends on the type of transition.

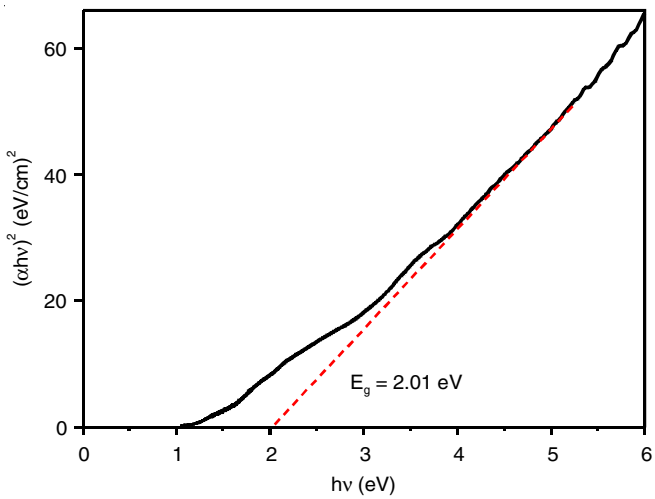

Fig. 5. Tauc plot of $CoFe_{12}O_{19}$ hexaferrite sample, prepared in presence of *Moringa oleifera* flowers extract

Magnetic measurement: Using a vibrating sample magnetometer (Lake Shore, Model 7410) at 300 K with an applied field of ± 15 kOe, the M-H loop of $CoFe_{12}O_{19}$ ferrite was measured as depicted in Fig. 6a, whereas Fig. 6b shows the initial magnetization curve.

The magnetic values provided in Table-2 were computed using a hysteresis loop. As an intrinsic property, saturation magnetization (M_s) exists. The saturation magnetization for the $CoFe_{12}O_{19}$ ferrite is observed to be 14.95 emu/g. Compared

TABLE-2
MAGNETIC PARAMETERS AT ROOM TEMPERATURE, MAGNETIC MOMENTS OF $CoFe_{12}O_{19}$ SAMPLE

Sample	M_s (emu/g)	H_c (Oe)	M_r (emu/g)	M_r/M_s	$n_{B\ (\mu B)}$
$CoFe_{12}O_{19}$	14.94	1790.9	6.72	0.45	2.76

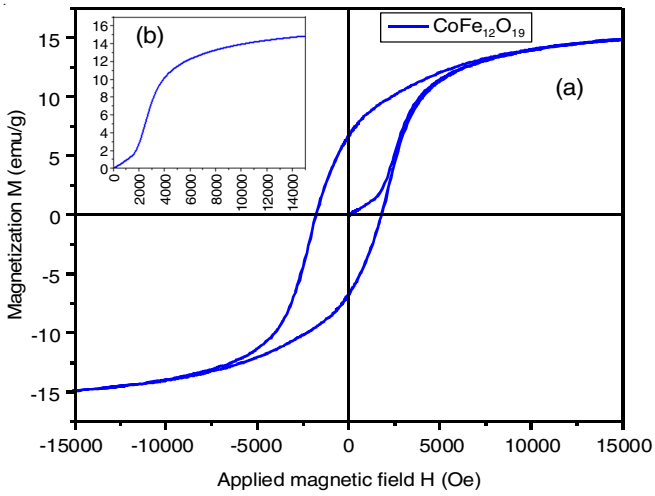

Fig. 6. MH hysteresis loop at room temperature of $CoFe_{12}O_{19}$ (CoM) sample

to the previously reported value (30.7 emu/g) [13], the prepared sample's saturation magnetization is lower. The non-magnetic hematite phase (and magnetic cobalt ferrite) present in the sample must be the key cause for the difference in the M_s value. The remanence magnetization value for the sample is 6.72 emu/g, which matches the reported values [13]. The coercivity H_c-value is 1790.0 Oe. Considered to be the most important factor in determining the magnetic characteristics is the squareness ratio (M_r/M_s). M_r/M_s is reported to be $0.45 < 0.5$ in the current example, showing magnetostatic interactions between the particles generating a multi-domain structure. The trapping of domain wall causes coercivity. In present case, the value of H_c (1790.9 Oe) is much higher than the reported values CoM (570 Oe) [13]. The multi-domain structure and the free easy domain walls movement may be the reason for the higher value of coercivity. The potential applications of $CoFe_{12}O_{19}$ with high coercivity (H_c) and low saturation magnetization (M_s) and remanence (M_r) are in inductor core, electromagnets, transformers and relays.

The magnetic moment in Bohr's magneton was calcuted using the following equation:

$$\eta_B = \frac{\text{Molecular weight} \times M_s}{5586} \quad (2)$$

where M is the molecular weight, M_s is the saturation magnetization.

Dielectric measurements

Variation of dielectric constant (real-ε′) with frequency: The dielectric characteristics were measured in the 20 Hz to 2 MHz frequency range at room temperature using an LCR metre (Agilent (E4980A)). Eqn. 3 was used to determine the dielectric constant's real portion:

$$\varepsilon' = \frac{C_p t}{\varepsilon_0 A} \quad (3)$$

where C_p, t, A and 0, respectively, stand for capacitance, the thickness of the pellet, its area and its permittivity in free space (8.854×10^{-12} F/m). Fig. 7a shows variation of ε′ with frequency for CoM ferrite sample. The dielectric properties of materials depend upon various factors like amount of dopants, particle size, cationic distributions, synthesis technique and time, *etc.* [17,18].

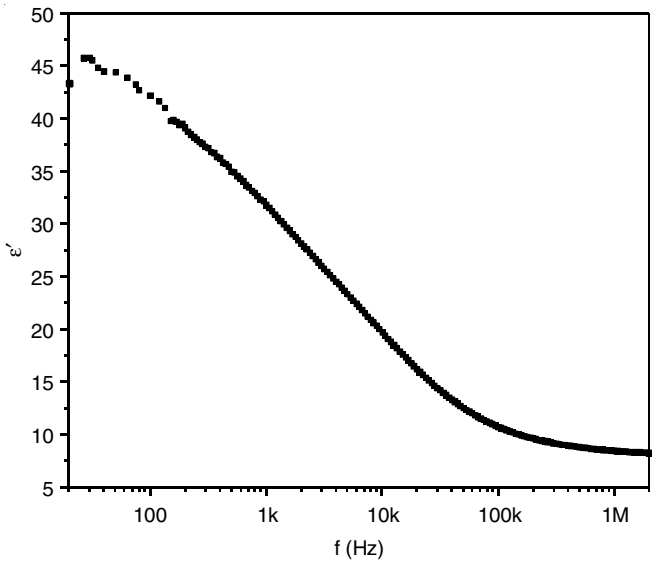

Fig. 7a. Variation of dielectric constant with frequency of $CoFe_{12}O_{19}$ sample

The outcome shows that the real dielectric constant falls off with frequency (Fig. 7a), which is consistent with previous observations in ferrimagnetic materials [19-21]. This frequency dependence of the dielectric constant can be explained by Maxwell-Wagner's bilayer theory [22]. This suggests that ferrite materials have the two levels of the dielectric structure. Strongly conducting grain boundaries in the top layer isolate grains with strong conductivity. Electrons assemble at these borders because to the electron hopping between Fe^{2+} and Fe^{3+} ions. However, because to their inability to synchronise with the applied frequency's alternating electric field, these electrons do not accumulate as much at grain boundaries, which causes polarization to diminish as a result. The lower dielectric constant at higher frequencies is the result of the polarization's decline at higher frequencies [23].

Frequency dependent dielectric constant (complex-ε″): Fig. 7b displays the change of complex dielectric constant [or dielectric loss (ε″)] with frequency of a sample of $CoFe_{12}O_{19}$ hexaferrite. The ion motion caused by the applied alternating electric field is represented by the dielectric loss as electric energy. The Koop's theory is followed, which shows that the dielectric loss decreases with increasing frequency [24]. The sample displays a relaxation peak between 2-8 kHz frequency region. The appearance of relaxation peak is due to the matching

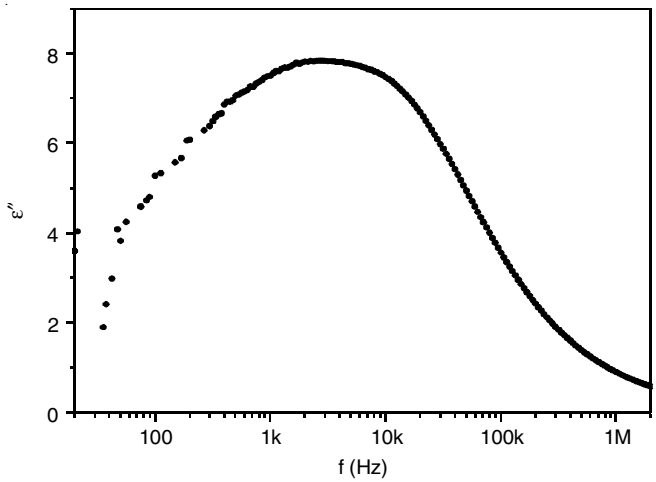

Fig. 7b. Complex dielectric constant variation with frequency of $CoFe_{12}O_{19}$ sample

of hopping frequency of ions with the externally applied frequency [25].

Variation of dielectric loss (tan δ) with frequency: The calculation of loss tangent (tan δ) value for prepare CoM sample was done using eqn. 4:

$$\tan\delta = \frac{1}{2\pi fRC} \quad (4)$$

where f, R and C, respectively, stand for the frequency being used, resistance and plate capacitance. The loss tangent's (tan δ) variation with frequency is depicted in Fig. 7c. Many variables, including as stoichiometry, sintering temperature and the quantity of charge carriers, affect the dielectric loss factor. For CoM, a hump is seen between 10 and 40 kHz and the dielectric loss tangent (tan δ) is seen to grow with frequency up to 30 kHz. The broadening of the dissipation curve for the CoM sample is caused by the alignment of the dipoles with the alternating field. Resonance peaks can also be detected when the hopping frequency and the externally applied frequency are in phase.

Changes in AC conductivity (σ_{ac}) with frequency: The calculation of AC conductivity was performed using eqn. 5:

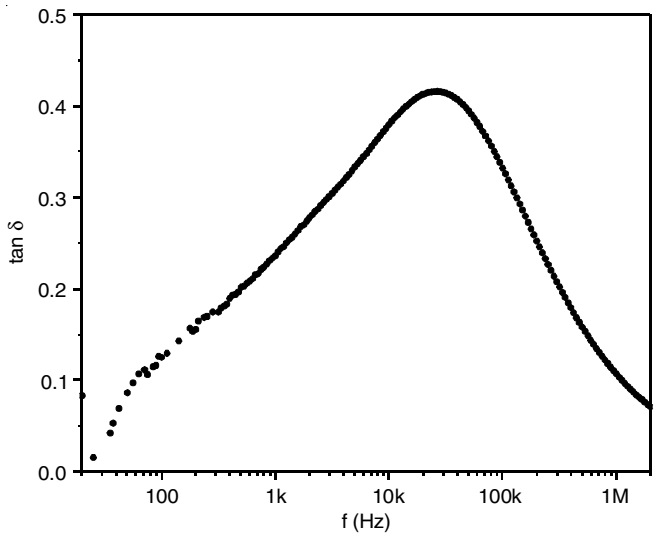

Fig. 7c. Dielectric loss tangent with frequency of $CoFe_{12}O_{19}$ sample

$$\sigma_{ac} = \omega\varepsilon'\varepsilon_0 \tan\delta \quad (5)$$

where, ω represents the angular frequency and ε_0 refers to the permittivity of free space or vacuum. The hopping of charge carriers for the same elements, which are present at several sites is the main contributor to conductivity in ferrite materials. Fig. 7d illustrates the changes in deviation of σ_{ac} with frequency for CoM ferrite sample. AC conductivity also rises as the frequency does. The Maxwell-Wagner theory states that grain boundaries function better at lower frequencies, which prevents electron hopping between Fe^{3+} and Fe^{2+} ions [26-28]. The maximum observed AC conductivity for the sample is 6.35×10^{-5} mho/cm.

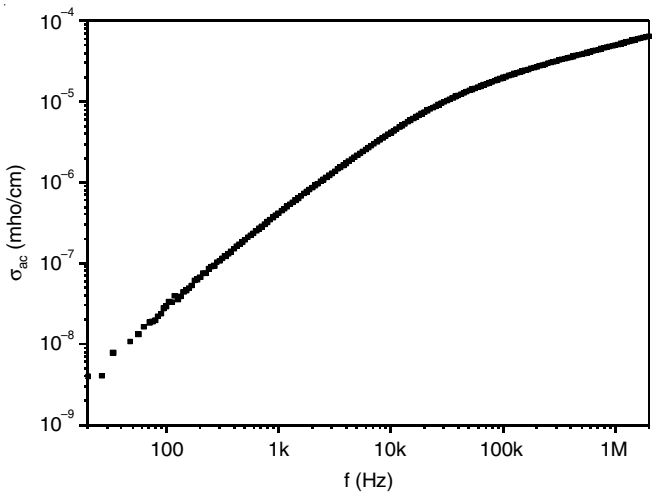

Fig. 7d. AC conductivity of $CoFe_{12}O_{19}$ sample

Dielectric modulus and impedance as a function of frequency: The dielectric modulus is an important characteristic of a material, which can provide information on relaxation time and ion hopping rates [29]. The variation of $CoFe_{12}O_{19}$'s real (M′) and imaginary (M″) dielectric moduli as a function of frequency in the range of 20 Hz to 2 MHz is depicted in Fig. 8a-b. The values were calculated [28] using the following formulas:

$$M' = \frac{\varepsilon'}{(\varepsilon'^2 + \varepsilon''^2)} \quad (6)$$

and

$$M'' = \frac{\varepsilon''}{(\varepsilon'^2 + \varepsilon''^2)} \quad (7)$$

where the imaginary component of the dielectric constant is ε″ and the real componentis ε′. Due to the tiny contribution of electrons and the long-distance movement of chargecarriers, M′ is 0.022 at 20 Hz. A smooth plateau is seen up to 1 kHz, after which short-range charge carrier movement causes the value of M′ in the high-frequency zone to rise to 0.12.

To investigate a material's relaxation behaviour and grain boundary contribution, one can utilize a complex electric modulus. Fig. 8b illustrates the variation in imaginary dielectric modulus with frequency. Starting at 20 Hz, an increase in the value of M″ is seen, with a relaxation peak at a frequency of 75.7 kHz for the $CoFe_{12}O_{19}$ sample synthesized with *M. oleifera* flower extract. The value of M″ varied from 0.001 (at 20 Hz) to 0.028 (at ~ 75.7 kHz).

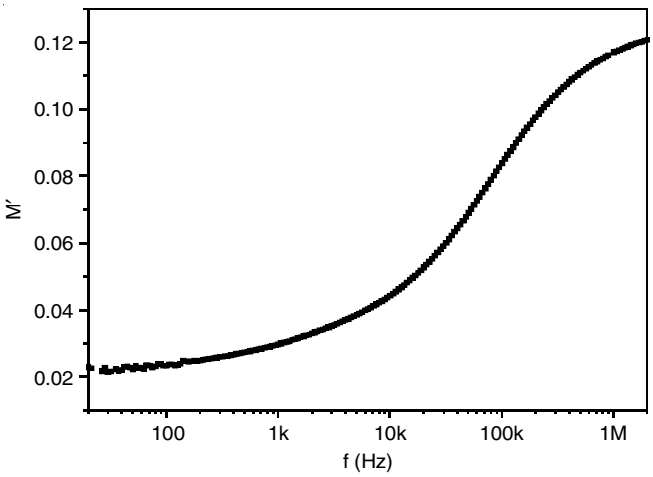

Fig. 8a. M′ variation with frequency for $CoFe_{12}O_{19}$ sample

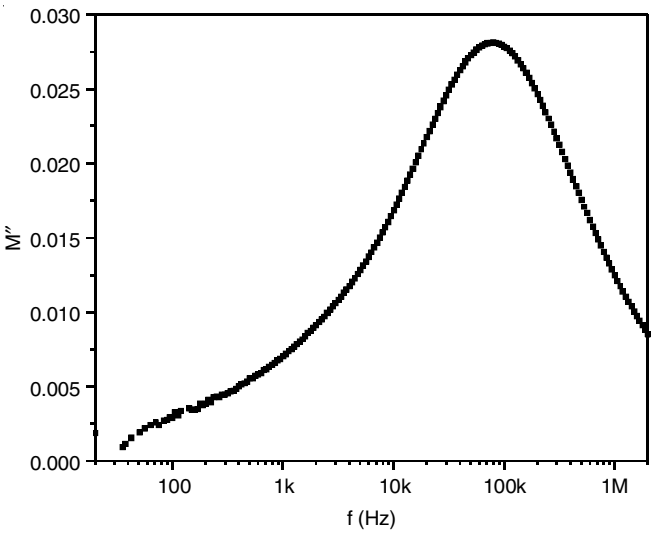

Fig. 8b. Variation of M″ as function of frequency of $CoFe_{12}O_{19}$ sample

The Cole-Cole plot (Fig. 8c) was plotted to investigate the reaction of the relaxation process. The provided sample shows a single full semicircle. The arc of this semicircle is compatible with the relaxation peak of the loss tangent (Fig. 7c). The grain's contribution to the high-frequency area is shown by arc.

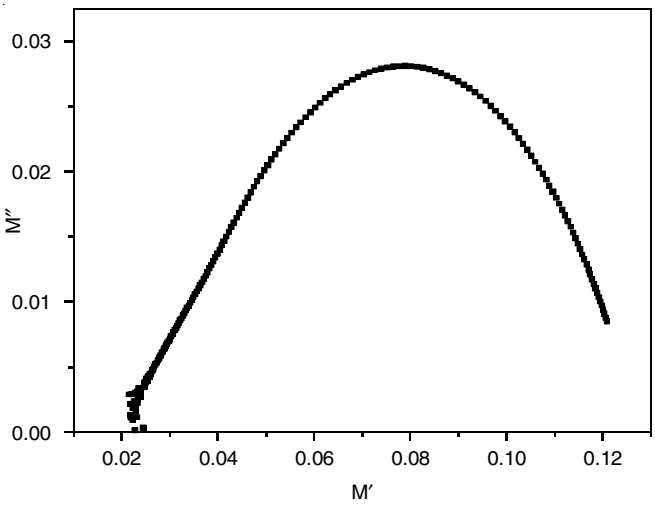

Fig. 8c. Cole-Cole plot of $CoFe_{12}O_{19}$ sample

The behaviour of frequency variation of impedance (Z′) is shown in Fig. 9a. A plateau after 100 kHz frequency indicates the lagging part of relaxation. With frequency increase, a decrease in impedance value is seen, which is associated with the production of space charge and lowering the energy barrier [28]. Impedance minimization is important for generating space charge and reducing energy barriers.

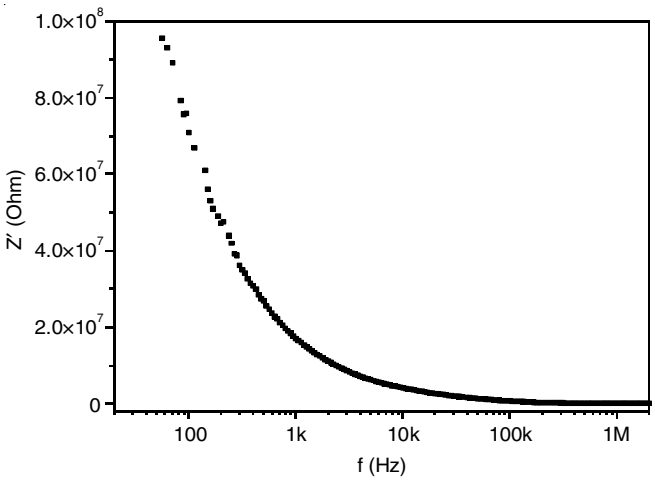

Fig. 9a. Real component of impedance (Z′) of $CoFe_{12}O_{19}$ sample

Impedance minimization is important for generating space charge and reducing energy barriers. Fig. 9b depicts the imaginary portion of the dielectric impedance as a function of frequency and Z″ decreases as frequency rises. The maximum value of Z″ found to be 2.8×10^9 ohm at 20 Hz. The imaginary part of dielectric impedance (Z″) is observed to be decreasing with the increase in frequency.

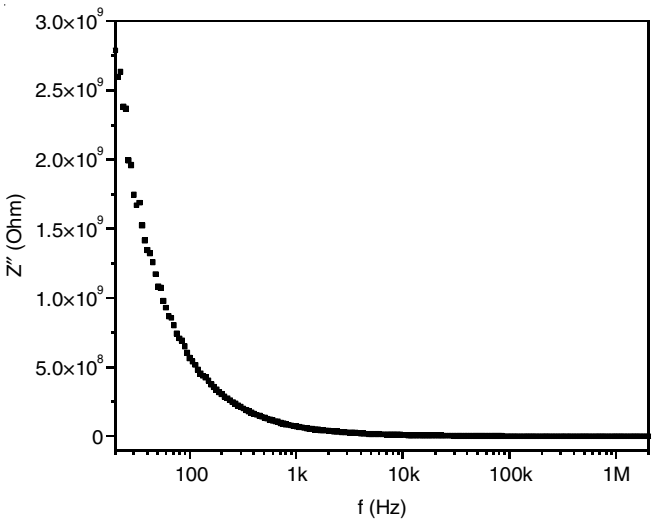

Fig. 9b. Imaginary component of impedance (Z″) of $CoFe_{12}O_{19}$ sample

Conclusions

$CoFe_{12}O_{19}$ hexaferrite powder was synthesized and characterized in the presence of *Moringa oleifera* flowers extract using FTIR, XRD, UV-VIS-NIR absorbance spectra, SEM,

VSM and dielectric techniques. The XRD investigation reveals the formation of M-phase (50%) along with α-Fe_2O_3 (31.25%) and $CoFe_2O_4$ (18.75%) phases and the cryatallite size was found to be 12.04 nm, while the energy bandgap was 2.01 eV. The SEM micrographs depicts the hexagonal shaped platelet like structure. The VSM results indicated the hard magnetic nature of the synthesized powder. The present hexaferrite has a saturation magnetization of 14.94 emu/g, remanence magnetization 6.72 emu/g and coercivity 1709.9 kOe. The composition possess multi-domain structure and the dielectric properties follow the Koop's model and Maxwell-Wagner theory where the dielectric constant $\varepsilon'_{max} \sim 46$ found at 30 Hz frequency and the relaxation peak of the loss tangent is consistent with the semicircle arc observed in the Cole-Cole plot.

ACKNOWLEDGEMENTS

One of the authors, C.C. Chauhan is thankful to GUJCOST, Gandhinagar, India for the financial support. Another author, R.B. Jotania is grateful to UGC, New Delhi, India for DRS-SAP-Phase–II (F.530/10/DRS/2018 (SAP-I) dated 17th April 2018) and DST, India for DST-FIST (level- I, No. SR/FST/PSI-198/2014) for providing grants.

CONFLICT OF INTEREST

The authors declare that there is no conflict of interests regarding the publication of this article.

REFERENCES

1. Y. Mizuno, S. Taruta and K. Kitajima, *J. Mater. Sci.*, **40**, 165 (2005); https://doi.org/10.1007/s10853-005-5702-5
2. R.C. Pullar, *Prog. Mater. Sci.*, **57**, 1191 (2012); https://doi.org/10.1016/j.pmatsci.2012.04.001
3. V.P. Singh, R. Jasrotia, R. Kumar, P. Raizada, S. Thakur, K.M. Batoo and M. Singh, *World J. Conden. Matt. Phys.*, **8**, 36 (2018); https://doi.org/10.4236/wjcmp.2018.82004
4. G. Oza, A. Reyes-Calderón, A. Mewada, L.G. Arriaga, G.B. Cabrera, D.E. Luna, H.M.N. Iqbal, M. Sharon and A. Sharma, *J. Mater. Sci.*, **55**, 1309 (2020); https://doi.org/10.1007/s10853-019-04121-3
5. N.Z. Abd Rani, K. Husain and E. Kumolosasi, *Front. Pharmacol.*, **9**, 108 (2018); https://doi.org/10.3389/fphar.2018.00108
6. M.R. Bindhu, M. Umadevi, G.A. Esmail, N.A. Al-Dhabi abd M.V. Arasu, *J. Photochem. Photobiol. B: Biol.*, **205**, 111836 (2020); https://doi.org/10.1016/j.jphotobiol.2020.111836
7. P. Virk, Manal A. Awad, S.S. Abdu-llah Alsaif, A.A. Hendi, M. Elobeid, K. Ortashi, R. Qindeel, M.F. El-Khadragy, H.M. Yehia, M.F.S. El-Din and H.A. Salama, *J. King Saud Univ. Sci.*, **35**, 102576 (2023); https://doi.org/10.1016/j.jksus.2023.102576
8. J.S. Moodley, S.B.N. Krishna, K. Pillay, Sershen and P. Govender, *Adv. Nat. Sci: Nanosci. Nanotechnol.*, **9**, 015011 (2018); https://doi.org/10.1088/2043-6254/aaabb2
9. A. Venkatachalam, J.P. Jesuraj and K. Sivaperuman, *J. Chem.*, **2021**, 4301504 (2021); https://doi.org/10.1155/2021/4301504
10. M.S. Kiran, C.R. Rajith Kumar, U.R. Shwetha, H.S. Onkarappa, V.S. Betageri and M.S. Latha, *Chem. Data Coll.*, **33**, 100714 (2021); https://doi.org/10.1016/j.cdc.2021.100714
11. M.M. Haque, M. Huq and M.A. Hakim, *Mater. Chem. Phys.*, **112**, 580 (2008); https://doi.org/10.1016/j.matchemphys.2008.05.097
12. Ravleen, S.K. Godara, B. Kaur, V. Kaur, A.K. Sood, P.S. Malhi, G. Ram Bhadu, I. Pushkarna and M. Singh, *Mater. Today Proc.*, **28**, 1 (2020); https://doi.org/10.1016/j.matpr.2019.12.056
13. F. Ansari, F. Soofivand and M. Salavati-Niasari, *Compos., Part B Eng.*, **165**, 500 (2019); https://doi.org/10.1016/j.compositesb.2019.02.010
14. C. Bohlender, M. Kahnes, R. Müller and J. Töpfer, *J. Mater. Sci.*, **54**, 1136 (2019); https://doi.org/10.1007/s10853-018-2916-x
15. M. Younas, M.H. Rasool, M. Khurshid, A. Khan, M.Z. Nawaz, I. Ahmad and M.N. Lakhan, *Biochem. Syst. Ecol.*, **107**, 104605 (2023); https://doi.org/10.1016/j.bse.2023.104605
16. J. Tauc, R. Grigorovici and A. Vancu, *Phys. Status Solidi, B Basic Res.*, **15**, 627 (1966); https://doi.org/10.1002/pssb.19660150224
17. G. Rana, U.C. Johri and K. Asokan, *Europhys. Lett.*, **103**, 17008 (2013); https://doi.org/10.1209/0295-5075/103/17008
18. Z.K. Heiba, M. Bakr Mohamed, A.M. El-naggar and A.A. Albassam, *Results Phys.*, **24**, 104116 (2021); https://doi.org/10.1016/j.rinp.2021.104116
19. A.M. Abo El Ata and M.A. Ahmed, *J. Magn. Magn. Mater.*, **208**, 27 (2000); https://doi.org/10.1016/S0304-8853(99)00547-8
20. A. Singh, S.B. Narang, K. Singh, P. Sharma and O.P. Pandey, *Eur. Phys. J. Appl. Phys.*, **33**, 189 (2006); https://doi.org/10.1051/epjap:2006016
21. M. Nyathani, G. Sriramulu, T.A. Babu, N.V. Prasad, D. Ravinder and S. Katlakunta, *Biointerface Res. Appl. Chem.*, **12**, 929 (2021); https://doi.org/10.33263/BRIAC121.929939
22. J.C. Maxwell, A Treatise on Electricity and Magnetism, Cambridge University Press (2010).
23. X. Li and G.L. Tan, *J. Alloys Compd.*, **858**, 157722 (2021); https://doi.org/10.1016/j.jallcom.2020.157722
24. C.G. Koops, *Phys. Rev.*, **83**, 121 (1951); https://doi.org/10.1103/PhysRev.83.121
25. B. Ahmad, S. Mumtaz, N. Karamat, R.S. Gohar, M.N. Ashiq and A. Shah, *J. Saudi Chem. Soc.*, **23**, 407 (2019); https://doi.org/10.1016/j.jscs.2018.06.008
26. A. Aslam, M.U. Islam, I. Ali, M.S. Awan, M. Irfan and A. Iftikhar, *Ceram. Int.*, **40**, 155 (2014); https://doi.org/10.1016/j.ceramint.2013.05.116
27. C.V. Ramana, Y.D. Kolekar, K. Kamala Bharathi, B. Sinha and K. Ghosh, *J. Appl. Phys.*, **114**, 183907 (2013); https://doi.org/10.1063/1.4827416
28. A. Gonchar, S. Gorelik, S. Katynkina, L. Letyuk and I. Ryabov, *J. Magn. Magn. Mater.*, **215–216**, 221 (2000); https://doi.org/10.1016/S0304-8853(00)00305-X
29. P.B. Macedo, C.T. Moynihan and R. Bose, *Phys. Chem. Glasses*, **13**, 171 (1972).